 doi:10.20944/preprints202008.0456.v1

Article

Hydrogen Peroxide Detection by Super-Porous Hybrid CuO/Pt NP Platform: Improved Sensitivity and Selectivity

Rakesh Kulkarni, Sundar Kunwar, Rutuja Mandavkar, Jae–Hun Jeong* and Jihoon Lee**

Department of Electronic Engineering, College of Electronics and Information, Kwangwoon University, Nowon-gu Seoul 01897, South Korea.

Correspondence e-mail: myloveofjh@gmail.com, jihoonlee@kw.ac.kr**

Abstract: A super-porous hybrid platform can offer significantly increased number of reaction sites for the analytes and thus can offer advantages in the biosensor applications. In this work, a significantly improved sensitivity and selectivity of hydrogen peroxide (H_2O_2) cancer sensor is demonstrated by a super-porous hybrid CuO/Pt NP platform. The super-porous hybrid platform is fabricated by a physiochemical approach combining the physical vapor deposition of Pt NPs and electrochemical deposition of super-porous CuO structures by adopting a dynamic hydrogen bubble technique. Under an optimized condition, the hybrid CuO/Pt biosensor demonstrates a very high sensitivity of 2,205 μA/mM·cm^2 and a low limit of detection (LOD) of 140 nM with a wide range of H_2O_2 detection. This is meaningfully improved performance as compared to the CuO-based H_2O_2 sensors as well as to the previously reported metal oxide based H_2O_2 sensors. The hybrid CuO/Pt platform exhibits excellent selectivity against other interfering molecules such as glucose, fructose, dopamine, and ascorbic acid. Due to the synergetic effect of highly porous CuO structures and underlying Pt NPs, the CuO/Pt architecture offers extremely abundant active sites for the H_2O_2 reduction and electron transfer pathways.

Keywords: H_2O_2 detection, cancer detection, super-porous CuO/Pt electrode, dynamic hydrogen bubble technique, biosensor kit

1. Introduction

One of the most important health issues in the 21st century is the cancer detection [1]. There are almost 18 million cancer cases around the world according to the report by the World Cancer Research Fund International (www.wcrf.org) in 2018. Cancers are of many forms, such as lung, liver, prostrate, cervical, bladder, ovarian and breast and the costly diagnosis is required [2], [3]. To have the best chances for successful treatments, as early detection is crucial [4]. Hydrogen peroxide (H_2O_2) is commonly produced by the cancer cells [5], [6] and the increased level of H_2O_2 can indicate the growth of cancer cells and DNA damages [7], [8] as well as accelerated aging and neurological disorders [9]. Thus, the H_2O_2 detection is essential for the early diagnosis of cancers [6], [10]. Here, the being required is the high sensitivity, low limit of detection (LOD) and fast response.

Various techniques have bene developed for the H_2O_2 detection including the colorimetric assay, fluorescence detection [11], electrochemical luminescence[8], SERS [12] etc. Among these, the electrochemical sensing [13] can offer one of the handiest approaches for the early detection of H_2O_2 due to its high sensitivity, fast response, precision and simple operation. The working principle of electrochemical H_2O_2 detection is based on the reduction of H_2O_2 into H_2O by the active electrode

Preprints (www.preprints.org) | NOT PEER-REVIEWED | Posted: 20 August 2020 doi:10.20944/preprints202008.0456.v1

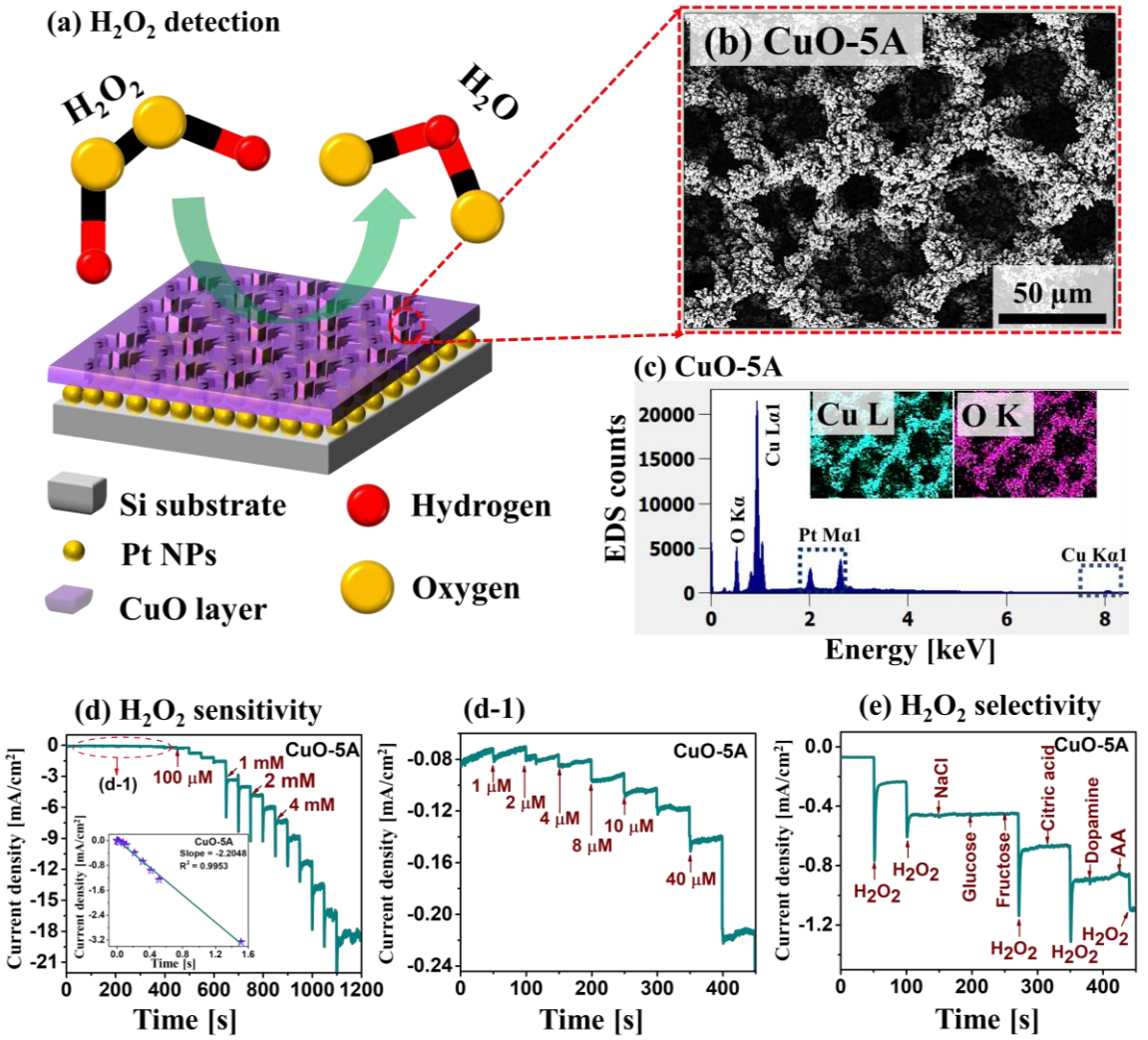

Figure 1. (a) Schematic representation of H_2O_2 detection by a super-porous hybrid CuO nanosturctures on Pt NPs (CuO/Pt) platform. (b) SEM image of typical porous CuO nanostructures. (c) Corresponding EDS spectra and elemental maps. (d) - (d-1) Amperometric response of CuO-5A sample upon the dropwise addition of H_2O_2 concentration from 1µM – 4 mM in a 0.1 M PBS solution of a pH 7.4 at - 0.4 V potential. (e) Selectivity response of CuO-5A upon the successive addition of 0.1 mM H_2O_2, NaCl, glucose, fructose, citric acid, dopamine and ascorbic acid (AA) to 0.1 M PBS (pH 7.4).

materials [9]. The sensitivity, selectivity and LOD of H_2O_2 sensing directly depend upon the morphological, electrical and catalytic properties of the sensing electrodes [14]. In terms of the electrode materials, recently, noble metallic nanoparticles (NPs) have gained much attentions in the H_2O_2 detection due to the small particle size, high surface area and high electrocatalytic activity [15]–[17]. At the same time, metal oxides such as CuO, NiO, MnO_2 and Ag_2O nanostructures have emerged as a new class of materials for the non-enzymatic electrochemical sensors [18-21]. Among various metal oxides, CuO as a p-type semiconductor having 1.2 eV bandgap can offer high stability, better electrochemical properties, and low manufacturing cost [19–21]. On the other hand, the Pt NPs are well known for their excellent catalytic activity and higher stability over other metals as well as high electrical conductivity [16], [22]. Thus, the combination of CuO structures such as highly porous CuO nanostructures on a Pt NP template could provide a significantly increased number of active sites and improved catalytic activity for the H_2O_2 reduction and efficient electron transfer pathways for the electrochemical detection.

Preprints (www.preprints.org) | NOT PEER-REVIEWED | Posted: 20 August 2020 doi:10.20944/preprints202008.0456.v1

In this work, a novel H_2O_2 sensing platform is demonstrated by super-porous hybrid CuO nanostructures on Pt NPs (CuO/Pt). The schematic representation of H_2O_2 molecule detection is represented in Fig. 1(a). The super-porous CuO/Pt hybrid electrode is demonstrated by a physical vapor deposition of Pt NPs followed by the electrochemical deposition of porous CuO nanostructures is shown in Fig. 1(b). The super-porous CuO nanostructures are fabricated by the dynamic hydrogen bubble technique, which enables the fabrication of highly porous CuO nanostructures rather than the films. Fig. 1(c) shows the EDS spectra for CuO-5A sample. The super-porous hybrid platform demonstrates a remarkably high sensitivity of 2,205 μA/mM·cm^2 for the H_2O_2 detection as seen in Fig. 1(d), and an excellent selectivity again glucose, fructose, dopamine, NaCl, Citric acid and ascorbic acid as clearly seen in Fig. 1(f). It also shows a low limit of detection (LOD) of 140 nM with a wide detection range. This is the first demonstration of super-porous CuO nanostructures and of the hybrid architecture with the Pt NPs for the H_2O_2 sensing.

2. Materials and Methods

2.1. Materials

Copper sulfate ($CuSO_4$), sulfuric acid (H_2SO_4), glucose ($C_6H_{12}O_6$), fructose ($C_6H_{12}O_6$), dopamine ($C_8H_{11}NO_2$), ascorbic acid (AA, $C_6H_8O_6$), sodium chloride (NaCl), hydrogen peroxide (H_2O_2), citric acid ($C_6H_8O_7$) and phosphate buffer saline tablets (PBS) were purchased from Sigma – Aldrich (United States). All the reagents were of analytical grade and used without further purification. Deionized (DI) water was used as a solvent throughout the experiment.

2.2. Fabrication of Pt NPs

Prior to the deposition of Pt on Si substrate, the Si substrate was degassed in the pulsed laser deposition (PLD) chamber under the 1.0×10^{-4} Torr at 725 ^oC for 30 min to remove the trapped gases, water vapors and contaminants. After degassing, the substrate was shifted to the plasma-assisted sputtering chamber for the deposition of 50 nm Pt film with the ionization current of 7 mA under 1.0×10^{-1} Torr. Subsequently, the Pt deposited Si sample was annealed in the PLD chamber at 425 ^oC for 30 minutes to enhance the adhesion of Pt on Si. During the annealing process, the chamber pressure was kept constant at 1.0×10^{-4} Torr and the temperature was increased at 4 ^oC/s to reach the target temperature. To finish the sample growth, the heating system was turned off and the sample was kept under the same vacuum until the temperature was dropped to an ambient over time. The surface morphology of the Pt/Si sample after the annealing process is shown in Fig. S1, which shows the RMS roughness (Rq) and surface area ratio (SAR) were much increased with the formation of Pt NPs.

2.3. Fabrication of CuO Nanostructures

The electrochemical deposition of Cu was carried out in a three-electrode system comprised of the Pt/Si substrate, platinum (Pt) electrode and Ag/AgCl electrode, as a working (WE), counter (CE) and reference (RE) electrodes respectively. For the deposition of Cu on the Pt/Si, the precursor solution of 0.1 M $CuSO_4$ and 0.05 M H_2SO_4 was prepared in 20 ml DI water. Then, various Cu layers were deposited by varying the deposition time such as 5, 10, 20, 30 and 50 s at a fixed current density of 2 A/cm^2 and at the deposition current density of 0.5, 1, 3 and 5 A/cm^2. After the electrochemical deposition of the Cu layer, the samples were transferred to the PLD chamber for a stepwise annealing at 300 and 500 ^oC for 30 minutes each with the continuous O_2 (20 CC) flow rate. The PLD chamber vacuum was 1.7×10^{-1} Torr during the annealing under O_2 supply. After the completion of the annealing process, the pure Cu metal layer was converted into the CuO through oxidation [38]. Based on the variation of deposition time and current density, the CuO samples are named as CuO-10s, CuO-20s, CuO-30s, CuO-50s and CuO-0.5A, CuO-1A, CuO-2A, CuO- 3A and CuO-5A respectively.

2.4. Characterizations

Preprints (www.preprints.org) | NOT PEER-REVIEWED | Posted: 20 August 2020 doi:10.20944/preprints202008.0456.v1

The surface morphology of the prepared CuO/Pt/Si samples was characterized by a scanning electron microscope (SEM, COXEM CX-200, South Korea), an atomic force microscopy (AFM Park System Corp. XE-70, South Korea). For an elemental characterization of samples and energy-dispersive x-ray spectroscope (EDS, Noran System 7, Thermo Fisher, USA) was used under the spectral and imaging modes. For the measurement of Raman spectra, the UNIRAM II system (UniNanoTech Co.Ltd., South Korea) integrated with the 532 nm laser, spectrograph (ANDOR sr-500), charge-coupled detector (CCD) detector and various optics was utilized. All the electrochemical measurements were carried out with the Wizmac-1200Premium system (Wizmac, South Korea).

3. Results and discussion

Figure 2 shows the physical properties of super-porous CuO/Pt hybrid electrodes by the variation of deposition-duration during the electrochemical deposition of Cu at 2 A/cm^2 in a solution containing 0.1 M $CuSO_4$ and 0.05 M H_2SO_4. Initially, the Pt nanoparticle (NP) templates were fabricated by the sputtering of 50 nm Pt film on Si substrate and subsequent annealing. The tiny Pt NPs were fabricated after annealing as seen in the AFM top views and line-profile in Fig. 2(a) – 2(b-1). Indeed, the Rq and SAR were significantly increased after the formation of Pt NPs as shown in Fig. 2(c). With the annealing of Pt layers under high temperature and vacuum, the strong adhesion between Pt and Si can be achieved as well, which could further facilitate the adsorption of Cu atoms during the electrochemical deposition. Figures 2(d) - 2(g) show the SEM images of highly porous CuO. The zoom-in SEM images are shown in Figs. 2(d-1) - 2(g-1). It can be observed that the partially connected CuO dendrites were formed on the surface of Pt NP template when the deposition time was 10s in Fig. 2(d). As the deposition time was increased, it resulted in the interconnected porous structures due to the additional deposition of Cu atoms in Figs. 2(e) - 2(g). The porous nature of CuO nanostructures was due to the simultaneous deposition of Cu and generation of hydrogen bubbles as described in Fig. S2 [23]. Due to the large overpotential, the co-reduction process occurs, in which the Cu ions are reduced simultaneously with the H^+ as described by Eqs. (1) and (2) [19].

$$2H^+_{(aq)} + 2e^- \rightarrow H_2 \quad (1)$$

$$Cu^{2+}_{(aq)} + 2e^- \rightarrow Cu_{(s)} \quad (2)$$

The generation of hydrogen bubbles functions as a dynamic bubble template for the Cu deposition. The pore size was found to be increased with the deposition time due to the coalescence of Cu nanostructures. Meanwhile, the intensive dendrites and corn-like agglomerates were grown towards the interior of pores, resulting in the formation of highly porous 3D Cu nanostructures. The complete mechanism of CuO fabrication on Pt/Si substrate is shown in Fig. S2 and additional SEM images are provided in Figs. S3. The Cu particle size was not significantly affected as seen in Figs. 2(d-1) - 2(g-1).

Preprints (www.preprints.org) | NOT PEER-REVIEWED | Posted: 20 August 2020 doi:10.20944/preprints202008.0456.v1

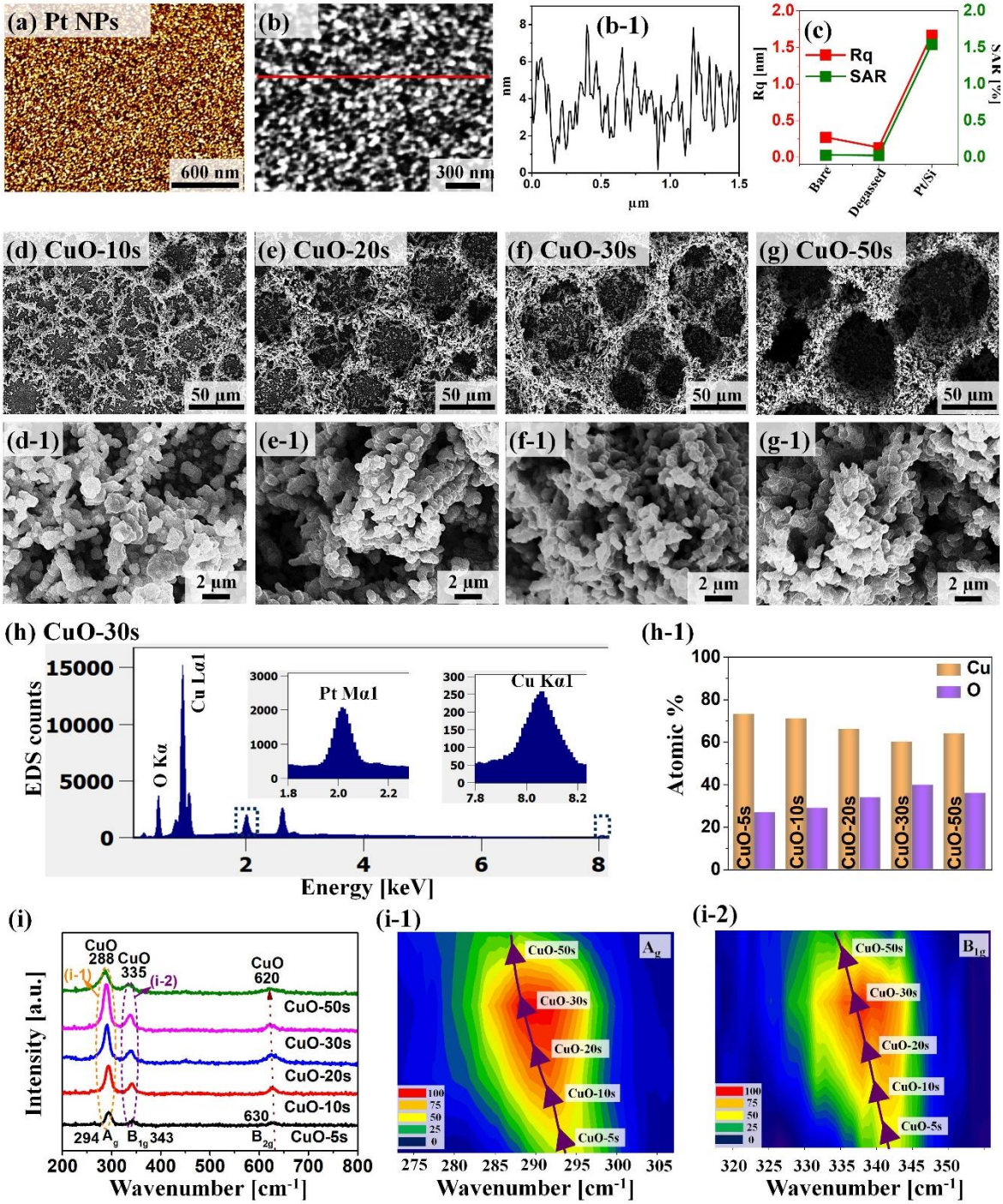

Figure 2. Structural analysis of porous CuO/Pt hybrid detectors fabricated at different deposition duration by an electrochemical deposition at 2 A/cm^2 cathodic current density in a solution of 0.1 M $CuSO_4$ and 0.05 M H_2SO_4. (a) AFM top-view of Pt NPs on Si substrate. (b) – (b-1) Magnified AFM top-view and corresponding cross-sectional line-profile. (c) Rq and SAR plots at different conditions. (d) – (g) SEM images of the porous CuO/Pt hybrid nanostructures for different deposition durations from 10 to 50s. The CuO-10s stands for the ten-second deposition duration**.** (d-1) – (g-1) Corresponding zoom-in SEM images. (h) EDS spectra of CuO-30s. (h-1) Summary of atomic percentage of Cu and O from different samples as a function of deposition time. (i) Raman spectra of the porous CuO/Pt hybrid samples. (i-1) – (i-2) Contour plots of the Raman peaks of CuO corresponding to the A_g and $B1_g$ modes.

Preprints (www.preprints.org) | NOT PEER-REVIEWED | Posted: 20 August 2020 doi:10.20944/preprints202008.0456.v1

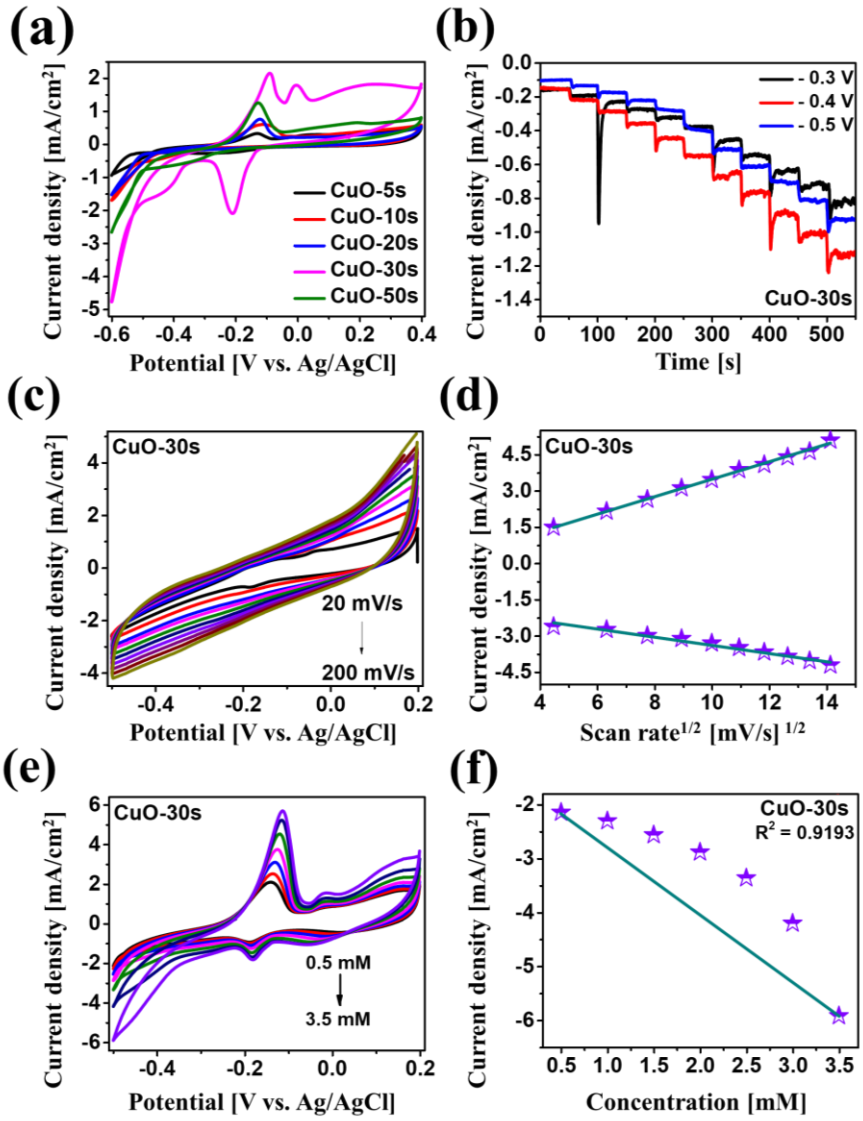

Figure 3. (a) Cyclic voltammetry (CV) response of various porous CuO/Pt hybrid detectors in 0.1 M PBS (pH 7.4) containing 0.4 mM H_2O_2 at a scan rate of 50 mV/s. (b) Amperometric response of CuO-30s sample with the dropwise addition of 0.1 mM H_2O_2 at different applied potential. (c) CVs response of the CuO-30s sample at different scan rates from 20 to 200 mV/s in 0.1 M PBS (pH 7.4) containing 0.1 mM H_2O_2. (d) Plot of oxidation and reduction peak current with respect to square root of scan rate. (e) CV of CuO-30s sample in 0.1 M PBS (pH- 7.4) containing different concentrations of H_2O_2 ranging from 0.5 to 3.5 mM at the scan rate of 50 mV/s. (f) Relation between peak current and H_2O_2 concentration.

Preprints (www.preprints.org) | NOT PEER-REVIEWED | Posted: 20 August 2020 doi:10.20944/preprints202008.0456.v1

After the fabrication of highly porous Cu nanostructures, each sample was annealed at 500 ^{o}C for 30 min with the O_2 (20 CC) flow, which oxidized the Cu into CuO without much difference in the morphology. Furthermore, the elemental characterization was carried out as shown in Figs. 2(h) – 2(h-1). The EDS spectra of other samples are provided in Figs. S4. The EDS spectra reveal the presence of Cu, O and Pt elemental peaks, indicating the formation of CuO on the Pt NP template. In addition, the corresponding atomic percentage of Cu and O for each sample is summarized in Fig. 2(h-1). This indicates that the oxygen amount was gradually increased up to 30 s of Cu deposition and the oxygen amount was decreased at 50 s likely due to the deposition of thicker Cu layer that prevents the exposure of Cu atoms during annealing under O_2. In addition, the Raman scattering spectra were measured for the CuO samples as shown in Figs. 2(i). All samples exhibited three Raman peaks at 294, 343 and 630 cm^{-1}, corresponding to the A_g, B_{1g} and B_{2g} phonon modes of CuO [24]. It was observed that the intensity of Raman peaks was gradually increased up to the CuO-30s, which may be due to the improved crystallinity of CuO. But, with the 50 s, a lower intensity of Raman peak was observed, which could be due to the poor crystallinity by an inefficient oxidation with the thick structure formation as discussed with the EDS spectra [25]. The counterplots of A_g and B_{1g} peaks are shown in Figs. 2(i-1) - 2(i-2), which demonstrate the blue shift of the A_g and B_{1g} Raman peaks and broadening. The gradual peak broadening and shift in the Raman peaks at ~ 288, 335 and 620 cm^{-1} can be due to the gradually increased size effect [26], [27]. When the deposition time was increased, the grain size was gradually increased, and the formation of thick CuO walls and formation of large dendrite structures were observed.

Figure 3 shows the electrochemical characterizations of the deposition-duration variation set via the cyclic voltammetry (CV) and the amperometry. First, the CV plots of CuO/Pt hybrid electrodes was measured in a stirred 0.1 M PBS (pH 7.4) containing 0.4 mM H_2O_2 at a scan rate of 50 mV/s as shown in Fig. 3(a). From the CV results, all the CuO samples showed a gradual increase in the oxidation and reduction peaks along with the deposition time up to 30s. With the increase in the deposition time, the CuO thickness was increased in both vertical and lateral directions, which resulted in the evolution of porous CuO nanostructures. Due to the much-increased thickness of Cu for the CuO-50s, the conversion rate of Cu to CuO was diminished, resulting in the increased atomic percentage of Cu as clearly demonstrated by the Raman and EDS spectra analyses in the previous section. The highly porous nature of the CuO-30s is not only effective for the electron pathways but also provides significantly increased number of active sites, which are helpful for the enhancement of electrochemical detection of H_2O_2. Generally, the overall mechanism of H_2O_2 reduction can be expressed by the relation [28]:

$$H_2O_2 + 2CuO \rightarrow Cu_2O + O_2 + H_2O \quad (3)$$

The electrocatalytic reduction of H_2O_2 by CuO can be described in two steps: (i) electrochemical reduction of Cu(II) to Cu(I) and (ii) electron transmission and O_2 generation, reducing the H_2O_2 into H_2O. From the CV measurement, the CuO-30s showed the high intense two reduction peaks at around - 0.2 and - 0.4 V and two oxidation peaks at - 0.1 and 0 V in Fig. 3(a). The two reduction peaks can be corresponded to the stepwise one-electron reduction of Cu(II) to Cu(I) and Cu(I) to Cu(0), whereas the two oxidation peaks can likely correspond to the one-electron oxidation of Cu(0) to Cu(I) and of Cu(I) to Cu(II) [29]. Since the CuO-30s demonstrated the highest oxidation and reduction peaks, it was further studied for the amperometric response at different applied potentials upon the drop-wise addition of 0.1 mM H_2O_2 solution as shown in Fig. 3(b). The maximum and stable current response was obtained at - 0.4 V. It is well known that applied potential in CA has a great influence on the sensitivity, stability and selectivity of the sensor [30]. Figure 3(c) displays the CV response of the CuO-30s by varying the scan rate in the range of 20 - 200 mV/s in a 0.1 M PBS (pH 7.4) containing 0.1 mM H_2O_2. With the higher applied scan rate, the peak potential was increased, which consequently indicates that the electrocatalytic activities are enhanced by the absorbed analytes at a higher scan rate. The corresponding anodic and cathodic peak currents are plotted based on the variation of the square root of the scan rate ($\upsilon^{1/2}$) as shown in Fig. 3(d), which indicates the linear relationship and thus signifies the characteristic of diffusion control electrochemical process [31]. Furthermore, the current versus potential relationship with the variation of H_2O_2 concentration

Preprints (www.preprints.org) | NOT PEER-REVIEWED | Posted: 20 August 2020 doi:10.20944/preprints202008.0456.v1

was studied at the scan rate of 50 mV/s as shown in Fig. 3(e). With the increased concentration of H_2O_2 from 0.5 to 3.5 mM, the current intensity of reduction and oxidation peaks were gradually increased due to the strong electrolyte reaction of H_2O_2. The increased reduction current can be ascribed to the increased Cu(II) species from Cu(I) by means of simultaneous reduction of H_2O_2 [19]. Fig. 3(f) shows the linear relation between the cathodic peak current and the concentration of H_2O_2 and the cathodic peak current increases progressively with the H_2O_2 concentration and hence indicating an excellent electrochemical activity of H_2O_2 reduction.

Figure 4 presents the CA response for the electrochemical detection of H_2O_2 by the CuO samples fabricated at different deposition time. The CA response was measured by a dropwise addition of H_2O_2 concentrations in an N_2-saturated 0.1 M PBS (pH 7.4) under a stirring condition at a potential of - 0.4 V. Fig. 4(a) shows the steady-state amperometric current response for the deposition time variation set upon the successive addition of 0.2 mM H_2O_2. The reduction current was sharply increased and stabilized approximately within 2 sec after the ingestion of H_2O_2 drop. Specifically, the CuO-30s demonstrated the highest current with a rapid electrochemical response among all samples. This can be due to the large active-surface area of porous CuO nanostructures that allows the diffusion of H_2O_2 molecules with the best crystalline quality and efficient electron transfer at the interface during the reduction process. Fig. 4(b) presents the current versus concentration relationship, in which the linear current response was observed as a function of concentration for all the samples and the CuO-30s exhibited the highest current difference. Moreover, various concentration of H_2O_2 was detected by the CuO-30s as displayed in Fig. 4(c), which demonstrates that the current response was sharply increased upon the addition of each drop of H_2O_2 from 1 μM to 4 mM. To gain a clear understanding of low concentration H_2O_2 detection, the concentration regime from 1 μM – 1.5 mM is separately plotted in Fig. 4(c-1), which displays a stepwise steady-state current after the successive addition of H_2O_2. In addition, Fig. 4(d) shows the linear calibration curve of current density versus H_2O_2 concentration ranging from 1 μM to 4 mM and Fig. 4(d-1) displays the linear regression described by equation (4) [12].

$$y = ax + b \ (R^2) \qquad (4)$$

$y = -1.4984\ x - 6.4111$ ($R^2 = 0.9976$) for the first linear range. The sensitivity is calculated to be 1498 μA/mM·cm^2 and the limit of detection (LOD) for the H_2O_2 is calculated to be 325 nM at a S/N ratio of 3 by equation (5) and (6), where, the σ represents the standard deviation [32].

$$S = \frac{slope}{area\ of\ (WE)} \qquad (5)$$

$$LOD = \frac{3 \times \sigma}{slope} \qquad (6)$$

Preprints (www.preprints.org) | NOT PEER-REVIEWED | Posted: 20 August 2020 doi:10.20944/preprints202008.0456.v1

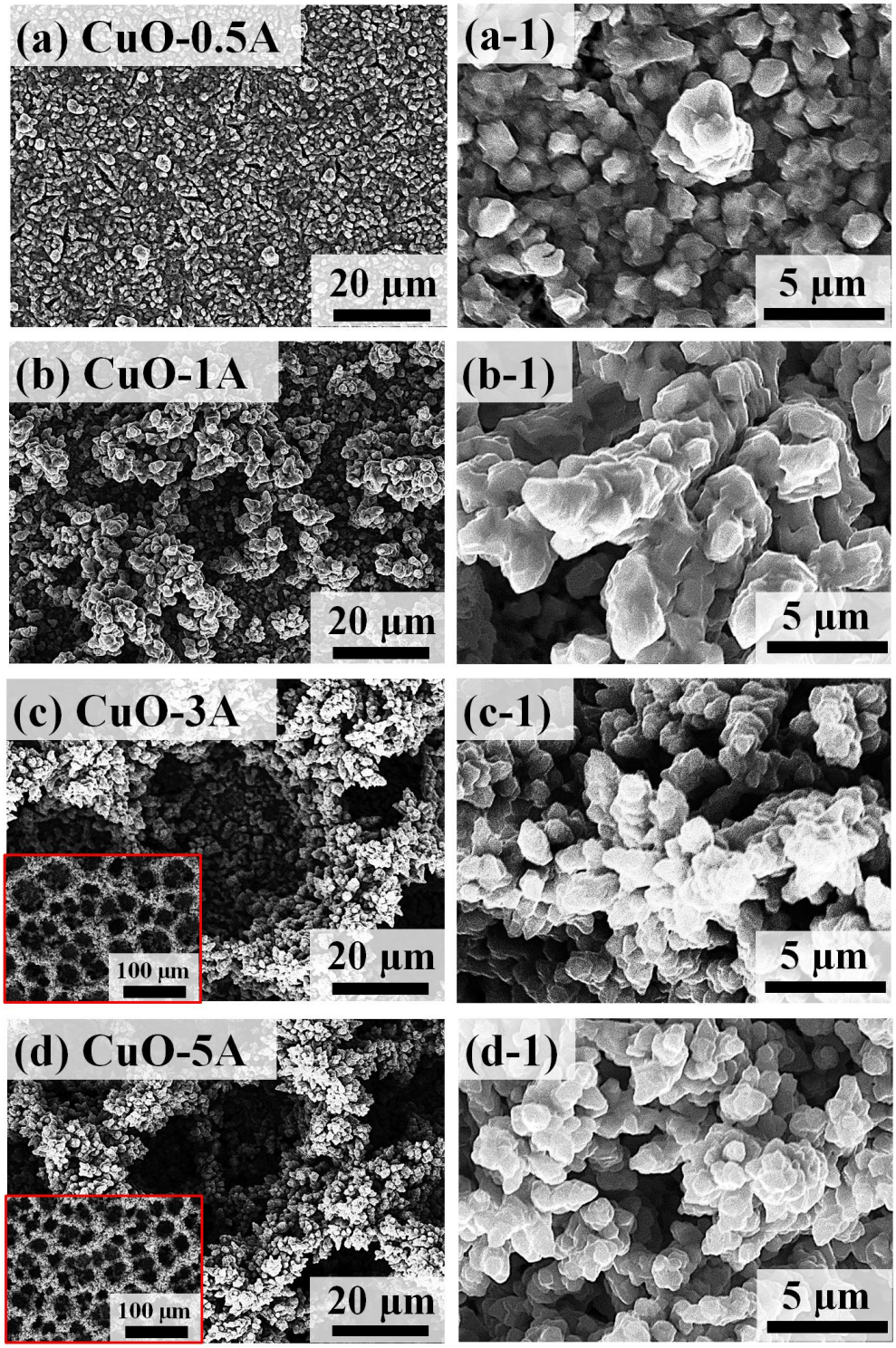

Figure 5. (a) – (d) SEM images of porous CuO nanostructures based on the control of current density between 0.5 and 5 A (CuO-0.5A – CuO-5A) for the fixed time of 30 s. (a-1) – (d-1) High magnification SEM images of the CuO nanostructures.

Preprints (www.preprints.org) | NOT PEER-REVIEWED | Posted: 20 August 2020 doi:10.20944/preprints202008.0456.v1

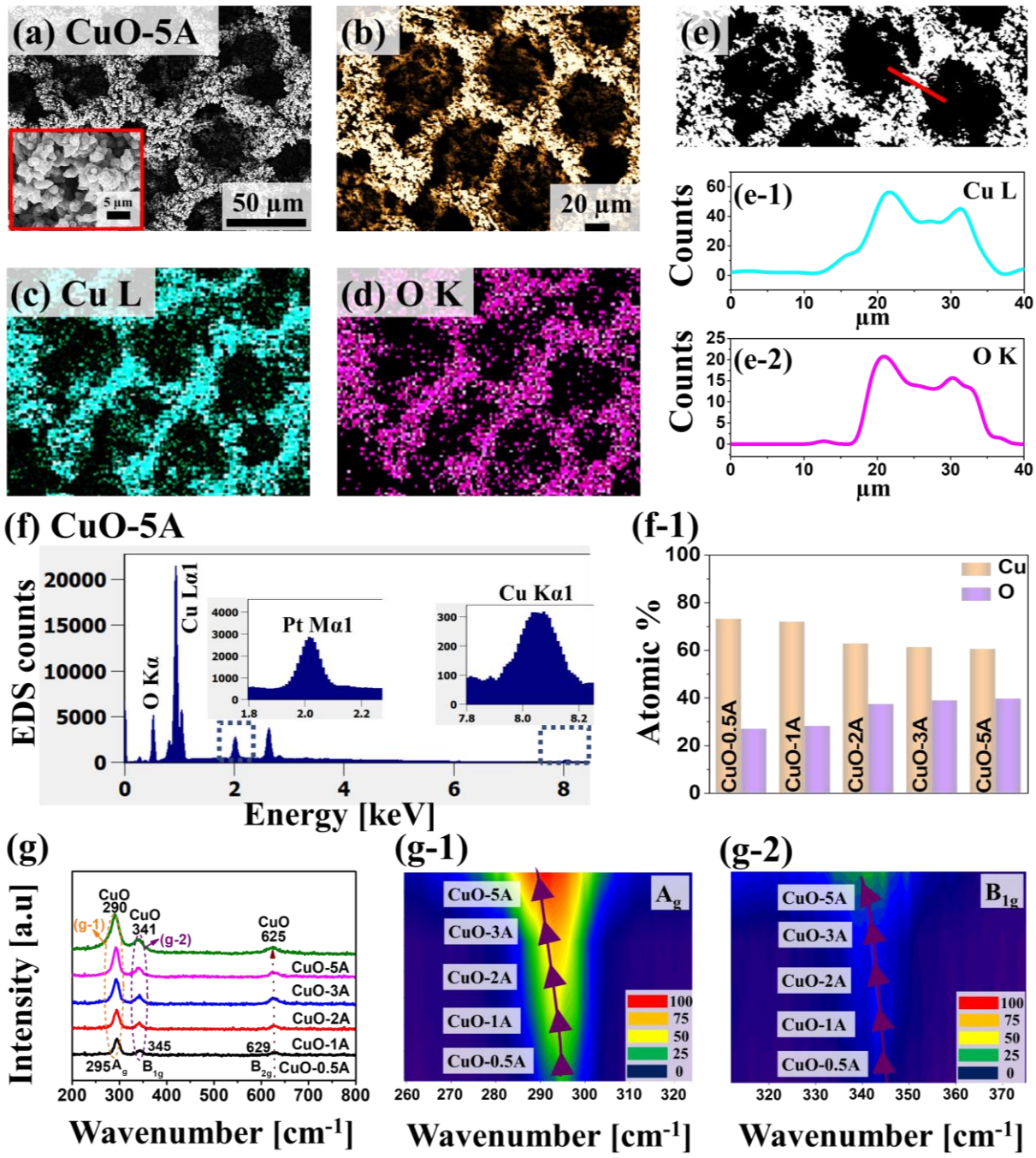

Figure 6. (a) SEM image of porous CuO/Pt hybrid detector fabricated at 5 A/cm^2 for 30 s and denoted as CuO-5A. (b) – (d) Enlarged SEM image and elemental maps of Cu and O for the CuO-5A. (e) – (e-2) Elemental line-profiles of Cu L and O K. (f) – (f-1) EDS spectra of CuO-5A and summary of atomic percentage of Cu and O as a function of deposition current. (g) Raman spectra for the porous CuO samples fabricated at different currents. (g-1) – (g-2) Contour maps of the Raman peaks of CuO corresponding to the A_g and $B1_g$ modes.

Preprints (www.preprints.org) | NOT PEER-REVIEWED | Posted: 20 August 2020 doi:10.20944/preprints202008.0456.v1

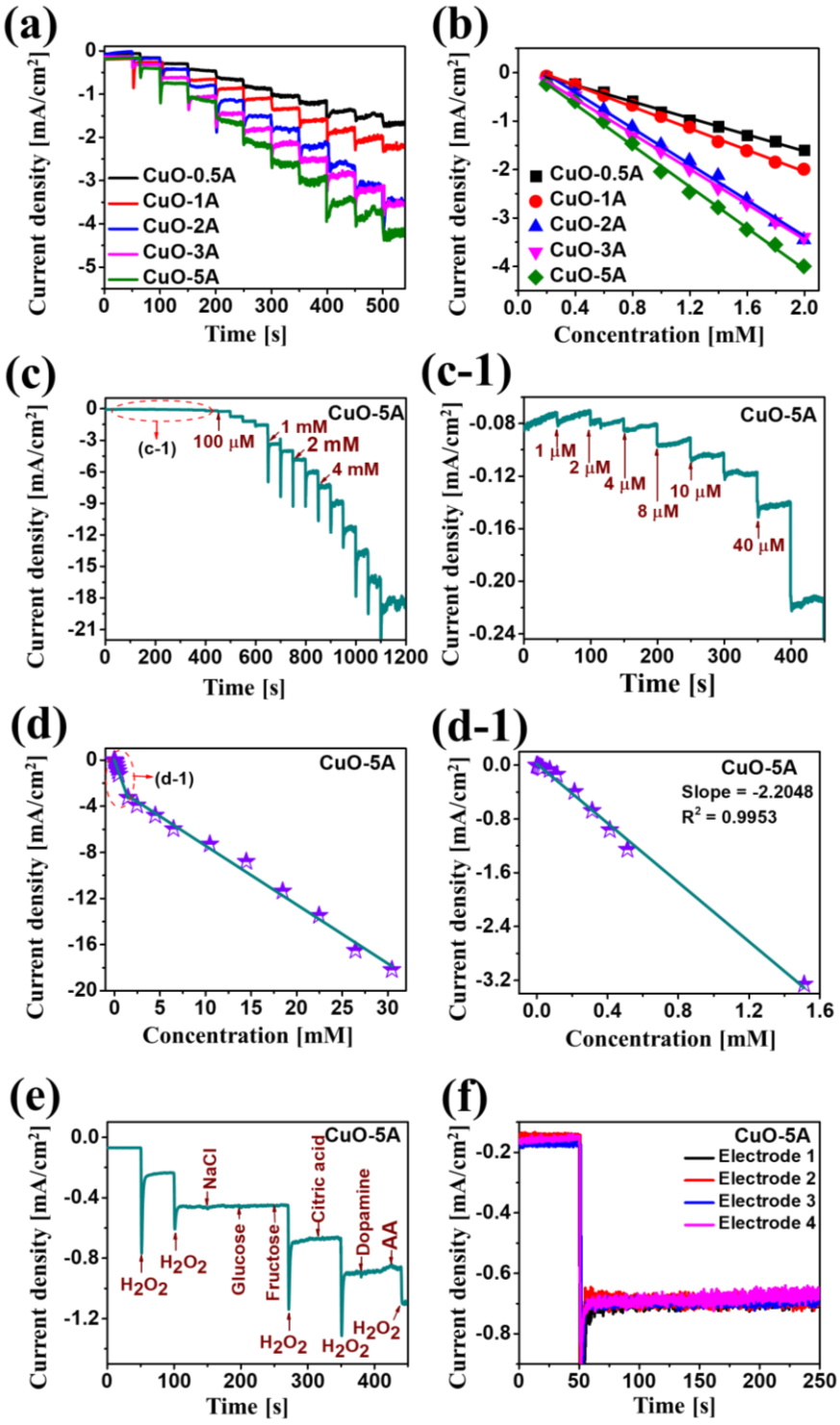

Figure 7. (a) Steady-state relation between current and time of current variation set upon successive addition of 0.2 mM H_2O_2 in the N_2 - saturated 0.1 M PBS (pH 7.4) at an applied potential of -0.4 V. (b) The corresponding calibration curves for H_2O_2 detection. (c) – (c-1) Amperometric response of CuO-5A upon dropwise addition of various H_2O_2 concentrations from 1 µM to 4 mM. (d) - (d-1) Calibration curve of current versus H_2O_2 concentration at different H_2O_2 concentration range. (e) Selectivity response of CuO-5A sample upon addition of 0.1 mM H_2O_2, NaCl, glucose, fructose, citric acid, dopamine, and ascorbic acid (AA) to 0.1 M PBS (pH 7.4). (f) Reproductivity test of CuO-5A samples 1 - 4 in the 0.1 M PBS (pH 7.4) at the potential of -0.4 V.

Preprints (www.preprints.org) | NOT PEER-REVIEWED | Posted: 20 August 2020 doi:10.20944/preprints202008.0456.v1

Figure 5 shows the physical characterization of porous CuO/Pt hybrid electrodes fabricated by the variation of current density between 0.5 and 5 A/cm^2 on Pt/Si substrate. The SEM images of CuO/Pt hybrid electrodes at different current densities are shown in Fig. 5. At a low current density of 0.5 and 1 A/cm^2, the discrete and irregular vertical growth of dendrite-like structures can be observed on the surface in Figs. 5(a) and 5(b). As the current density was increased further, more porous structures and large vertical dendrites are formed due to the abundant hydrogen bubble formation and clustering of electrodeposited metal atoms in Figs. 5(c) and 5(d). The morphology of porous structures directly depends upon the current density such that higher density and small pore size were obtained with higher current density, which can be due to the faster generation and desorption of hydrogen bubbles [33]. The CV and CA electrochemical response of these various CuO/Pt hybrid samples based on current density variation are presented in Fig. S7. From the CV and CA measurements, the electrochemical performance of CuO-5A for the H_2O_2 detection was found to be maximum in this set. Thus, the CuO-5A sample was further explored in terms of physical properties and electrochemical performance for the H_2O_2 detection. Figs. 6(a) - 6(d) show the SEM and EDS elemental maps of the CuO-5A respectively. The EDS elemental maps demonstrate the presence of Cu L and O K peaks in the CuO-5A and matches well with the SEM morphology. This clearly shows the co-existence of Cu and O elements in the porous nanostructures. In addition, the corresponding EDS line-profile analysis of the selected area is shown in Figs. 6(e) – 6(e-2), which confirms the uniform distribution of Cu and O in the nanostructures. The EDS spectrum of the porous CuO-5A sample in Fig. 6(f) also confirms the presence of Cu, O and Pt elements in the sample. From the atomic percentage plot in Fig. 6(f-1), the at. % of Cu was gradually reduced while the at. % of O was increased with the increased current density. This indicates that the amount of oxidized Cu is more with the high current density samples likely due to the higher porosity and pore density. The EDS elemental spectra of other samples in this set are provided in Fig. S6. To gain the structural insight, the Raman spectra analysis was performed as shown in Fig. 6(g). Generally, the Raman vibration peaks were observed at 295, 345 and 629 cm^{-1} for all CuO samples, which corresponds to A_g, B_{1g} and B_{2g}. In comparison to the Raman peak of the single crystal of CuO, the Raman peaks showed a gradual blue shift with a broadening as shown in Figs. 6(g-1) – 6(g-2). Again, this can be related to the increase grain size along with the increased current [26], [35].

Figure 7 shows the CA response of porous CuO/Pt hybrid electrodes fabricated at the controlled current density. The CA response was measured by the dropwise addition of H_2O_2 concentrations in the N_2-saturated 0.1 M PBS (pH 7.4) under the stirring condition at a potential of -0.4 V. Figure 7(a) shows the steady-state amperometric current response of samples upon the dropwise addition of 0.2 mM H_2O_2. In specific, the CuO-5A showed the highest current density under the same concentration of H_2O_2, indicating the superior diffusion of analyte due to the high porosity and crystallinity of CuO nanostructures. Fig. 7(b) presents the current versus concentration relationship, in which the linear current response was observed as a function of concentration for all the samples and the CuO-5A exhibited the highest current slop. Based on the high current response of the CuO-5A sample, it was further examined for the electrochemical H_2O_2 detection. The amperometric response of CuO-5A upon the dropwise addition of H_2O_2 from 1 μM to 4 mM is presented in Fig. 7(c), which clearly showed the current increment upon the addition of H_2O_2. The low concentration H_2O_2 detection between 1 and 40 μM was further plotted as shown in Fig. 7(c-1), which presents the steady and stable stepwise current state after the addition of H_2O_2. Furthermore, Fig. 7(d) shows the linear calibration curve of current density versus H_2O_2 concentration ranging from 1 μM to 4 mM. Fig. 7(d-1) displays the corresponding linear curve of current versus H_2O_2 concentration, the linear equation is given by equation (4), $y = -2.2048\ x - 0.339$ ($R^2 = 0.9953$) for the first linear range and the sensitivity is calculated to be about 2205 μA/mM·cm^2 and LOD is 140 nM [32]. Fig. 7(e) shows the selectivity characterization of the CuO-5A sample by varying the various organic molecules of 0.1 mM concentration, i.e. NaCl, glucose, fructose, citric acid, dopamine, and ascorbic acid (AA). Interestingly, no current response was observed with the addition of other organic molecules than H_2O_2. The alternated molecules dropping sequence showed that the current was sharply increased only for the addition of H_2O_2. This result clearly confirms that the CuO-5A is highly selective for the H_2O_2 detection at - 0.4 V applied bias against typical organic molecules. Furthermore,

Preprints (www.preprints.org) | NOT PEER-REVIEWED | Posted: 20 August 2020 doi:10.20944/preprints202008.0456.v1

the stability and reproductivity tests were conducted with the working electrode CuO-5A as shown in Fig. 7(f). During the 250 s test period, all four CuO-5A electrodes exhibited similar and stable current density upon the injection of the same concentration of H_2O_2. Thus, the porous CuO/Pt hybrid electrodes can be a promising platform for the fabrication of H_2O_2 detectors with the high sensitivity, selectivity and reproductivity. This can be attributed to the effective absorption of the H_2O_2 on the super-porous CuO interface and fast charge transport pathways through the underlying Pt NPs during the electrolysis process [36].

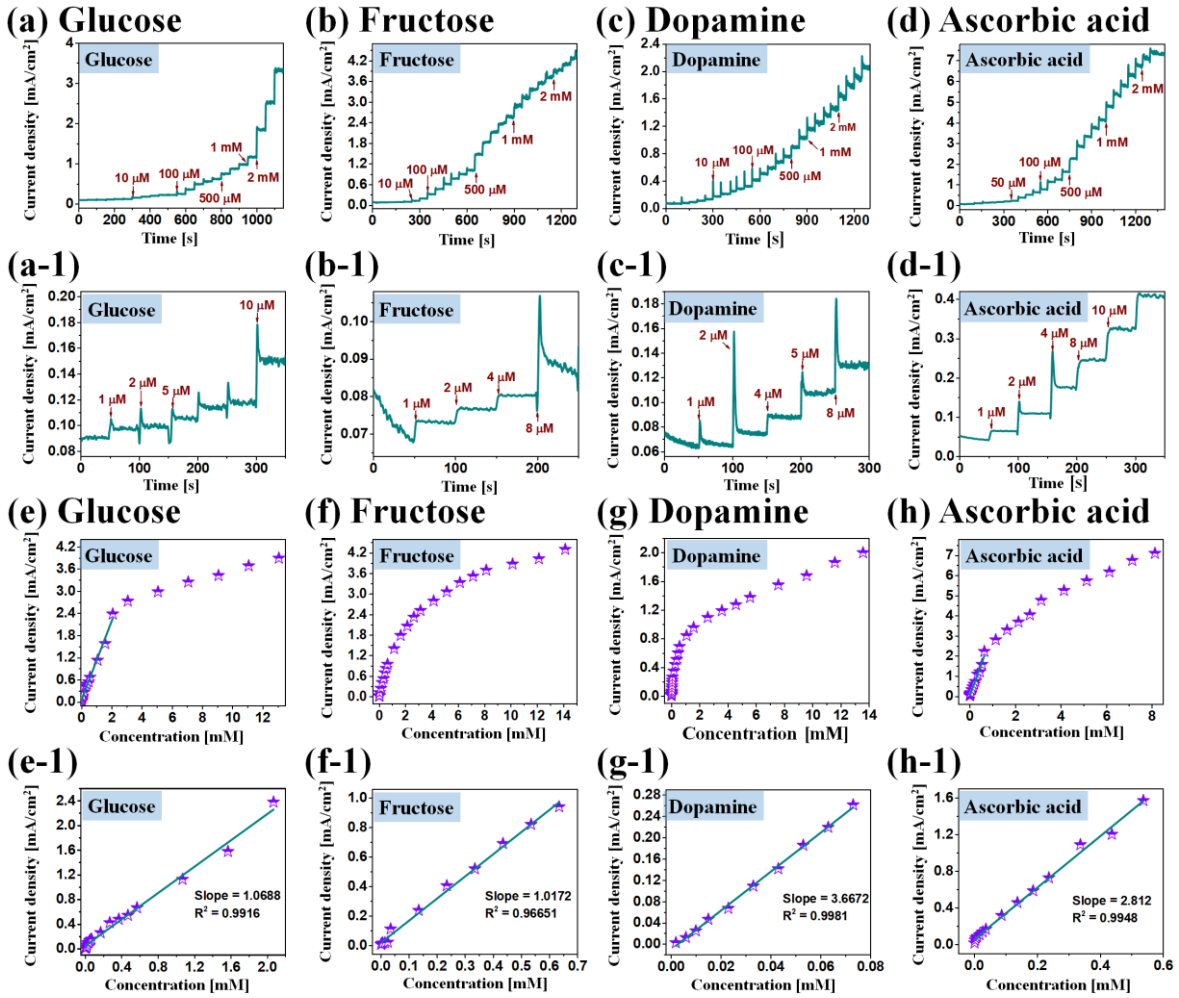

Figure 8. Amperometric response of CuO-5A sample upon dropwise addition of (a) glucose into 0.1 M NaOH at a potential of 0.6 V, (b) fructose into 0.1 M NaOH at a potential of 0.4 V, (c) dopamine into 0.1 M PBS at a potential of 0.6 V and (d) ascorbic acid into 0.1 M NaOH at a potential of 0.5 V, respectively. (a-1) – (d-1) Amperometric response of glucose, fructose, dopamine, and ascorbic acid at lower concentrations. (e) – (h) Calibration curves CuO-5A based on the current density versus high concentration of glucose, fructose, dopamine, and ascorbic acid. (e-1) – (h-1) Linear calibration curve based on the current density versus low concentration of glucose, fructose, dopamine, and ascorbic acid.

 doi:10.20944/preprints202008.0456.v1

Figure 8 presents the typical amperometric responses of CuO-5A for the detection of different organic molecules at different measurement conditions such as (a) glucose in 0.1 M NaOH at 0.6 V (b) fructose in 0.1 M NaOH at 0.4 V (c) dopamine in 0.1 M PBS at 0.6 V and (d) ascorbic acid in 0.1 M NaOH at 0.5 V. All the measurements were carried out the under N_2 saturation and stirring condition. Since, the applied potential has a great impact on the sensitivity, stability and selectivity of sensors, the applied potential for different molecules was determined based on the CV and CA measurement as shown in Fig. S8 [37]. Figures 8(a) – 8(d) show the amperometric response of CuO-5A sample upon the dropwise addition of different molecules as labeled with various concentrations ranging from 1 μM to 2 mM. Figures 8(a-1) – 8(d-1) present the magnified section of Figs. 8(a) – 8(d) at low concentration ranging from 1 – 10 μM. It was found that the CuO-5A sample exhibited a decent current response with the consequent step change for each drop of different molecules at different potentials. These results confirm that the porous CuO/Pt hybrid electrodes can exhibit excellent sensitivity with different organic molecules, which can be ascribed to high electroconductivity and good electrocatalytic activity. The corresponding linear calibration curves of current density versus concentration of each molecules at high concentration ranging from 10 μM to 2 mM is shown in Figs. 8(e) – 8(h). Similarly, the low concentration 1 – 10 μM linear calibration curves are presented in Figs. 8(e-1) – 8(h-1) for different molecules as labeled. From these results, it can be concluded that the porous CuO/Pt hybrid electrodes can be applied for the detection of various organic molecules at different applied potentials as well.

4. Conclusions

In summary, a significantly improved H_2O_2 detection performance has been demonstrated by the uniquely designed super-porous hybrid nanostructures of CuO/Pt on Si fabricated by the combined physicochemical approach. In particular, the physical vapor deposition of Pt NPs on the Si substrate was followed by the electrochemical deposition of highly porous nanostructures of CuO by the dynamic hydrogen bubbles approach at different deposition time and current densities. It has been found that the performance of the H_2O_2 sensor is highly dependent on deposition conditions. The highly porous structure CuO deposited at a current density of 5 A/cm^2 for 30s (CuO-5A) showed the best performance with the highest sensitivity, wide linear range and selectivity towards the H_2O_2. **Under the optimized conditions, the** CuO-5A **demonstrate**d the **sensitivity** of 2205 μA/mM·cm^2 with the wide detection range. It also showed demonstrated an excellent selectivity against other organic molecules like glucose, fructose, dopamine and ascorbic acid along with the **limit of detection of** 140 nM. The enhanced sensing performance was due to the increased active sites and improved H_2O_2 adsorption and interfacial electron transport, which was achieved by a unique manufacturing method of dynamic hydrogen bubble technique. Furthermore, the CuO-5A showed the detection of other organic materials at different applied potential. This work demonstrates that the highly porous CuO/Pt platform could be a promising candidate to develop an efficient electrochemical biosensor for the H_2O_2 sensor application.

Supplementary Materials: The following are available online at www.mdpi.com/xxx/s1, the Supplementary Materials includes the additional morphological, elemental and electrochemical characterizations of samples, including the AFM and SEM images, EDS spectra, cyclic voltammetry and amperometric responses.

Author Contributions: R.K. S.K. R.M J.J. and J.L. participated in the experiment design and carried out the experiments. R.K. S.K. R.M J.J. and J.L. participated in the characterizations and analysis of data. J.J. and J.L designed the experiments and testing methods. R.K. S.K. and J.L. carried out the writing. All authors helped in drafting and read and approved the final manuscript.

Funding: Financial support from the National Research Foundation of Korea (NRF) Grant funded by the Korean Government (MSIP) (no. NRF-2019R1A2C4069438 and NRF-2018R1A6A1A03025242) and in part by the research grant of Kwangwoon University in 2020 is gratefully acknowledged.

Conflicts of Interest: The authors declare no conflict of interest. The funders had no role in the design of the study; in the collection, analyses, or interpretation of data; in the writing of the manuscript, or in the decision to publish the results.

References

1. Lewandowska, A.M.; Rudzki, M.; Rudzki, S.; Lewandowski, T.; Laskowska, B. Environmental risk factors for cancer - review paper. *Ann. Agric. Environ. Med.* 2019, *26*, 1–7.
2. Barman, S.C.; Zahed, M.A.; Sharifuzzaman, M.; Ko, S.G.; Yoon, H.; Nah, J.S.; Xuan, X.; Park, J.Y. A Polyallylamine Anchored Amine-Rich Laser-Ablated Graphene Platform for Facile and Highly Selective Electrochemical IgG Biomarker Detection. *Adv. Funct. Mater.* **2020**, *30*, 1–10, doi:10.1002/adfm.201907297.
3. Ahrensberg, J.M.; Fenger-Grøn, M.; Vedsted, P. Primary care use before cancer diagnosis in adolescents and young adults - A nationwide register study. *PLoS One* **2016**, *11*, 5–6, doi:10.1371/journal.pone.0155933.
4. Maltser, S.; Cristian, A.; Silver, J.K.; Morris, G.S.; Stout, N.L. A Focused Review of Safety Considerations in Cancer Rehabilitation. *PM R* **2017**, *9*, S415–S428, doi:10.1016/j.pmrj.2017.08.403.
5. Zhang, T.; Lu, Y.; Luo, G. Synthesis of hierarchical iron hydrogen phosphate crystal as a robust peroxidase mimic for stable H2O2 detection. *ACS Appl. Mater. Interfaces* **2014**, *6*, 14433–14438, doi:10.1021/am503708a.
6. Blackadar, C.B. Historical review of the causes of cancer. *World J. Clin. Oncol.* **2016**, *7*, 54–86, doi:10.5306/wjco.v7.i1.54.
7. Nosaka, Y.; Nosaka, A.Y. Generation and Detection of Reactive Oxygen Species in Photocatalysis. *Chem. Rev.* **2017**, *117*, 11302–11336, doi:10.1021/acs.chemrev.7b00161.
8. Babamiri, B.; Bahari, D.; Salimi, A. Highly sensitive bioaffinity electrochemiluminescence sensors: Recent advances and future directions. *Biosens. Bioelectron.* **2019**, *142*, 111530, doi:10.1016/j.bios.2019.111530.
9. Zhao, J.; Yan, Y.; Zhu, L.; Li, X.; Li, G. An amperometric biosensor for the detection of hydrogen peroxide released from human breast cancer cells. *Biosens. Bioelectron.* **2013**, *41*, 815–819, doi:10.1016/j.bios.2012.10.019.
10. Sitnikova, N.A.; Borisova, A. V.; Komkova, M.A.; Karyakin, A.A. Superstable advanced hydrogen peroxide transducer based on transition metal hexacyanoferrates. *Anal. Chem.* **2011**, *83*, 2359–2363, doi:10.1021/ac1033352.
11. Choi, Y.J.; Takahashi, K.; Misawa, N.; Hizawa, T.; Iwata, T.; Sawada, K. Multi-wavelength fluorescence detection of submicromolar concentrations using a filter-free fluorescence sensor. *Sensors Actuators, B Chem.* **2018**, *256*, 38–47, doi:10.1016/j.snb.2017.09.077.
12. Yang, H.; Wang, Z.; Li, C.; Xu, C. Nanoporous PdCu alloy as an excellent electrochemical sensor for H2O2 and glucose detection. *J. Colloid Interface Sci.* **2017**, *491*, 321–328, doi:10.1016/j.jcis.2016.12.041.
13. Lu, W.; Sun, Y.; Dai, H.; Ni, P.; Jiang, S.; Wang, Y.; Li, Z.; Li, Z. Direct growth of pod-like Cu2O nanowire arrays on copper foam: Highly sensitive and efficient nonenzymatic glucose and H2O2 biosensor. *Sensors Actuators, B Chem.* **2016**, *231*, 860–866, doi:10.1016/j.snb.2016.03.058.
14. Xu, S.; Zhang, X.; Wan, T.; Zhang, C. A third-generation hydrogen peroxide biosensor based on horseradish peroxidase cross-linked to multi-wall carbon nanotubes. *Microchim. Acta* **2011**, *172*, 199–205, doi:10.1007/s00604-010-0479-x.
15. Wilson, N.M.; Flaherty, D.W. Mechanism for the Direct Synthesis of H2O2 on Pd Clusters: Heterolytic Reaction Pathways at the Liquid-Solid Interface. *J. Am. Chem. Soc.* 2016, *138*, 574–586.
16. Huang, X.; Zhu, Y.; Yang, W.; Jiang, A.; Jin, X.; Zhang, Y.; Yan, L.; Zhang, G.; Liu, Z. A self-supported CuO/Cu nanowire electrode as highly efficient sensor for COD measurement. *Molecules* **2019**, *24*, doi:10.3390/molecules24173132.
17. Huang, Y.; Ferhan, A.R.; Dandapat, A.; Yoon, C.S.; Song, J.E.; Cho, E.C.; Kim, D.H. A Strategy for the Formation of Gold-Palladium Supra-Nanoparticles from Gold Nanoparticles of Various Shapes and Their Application to High-Performance H2O2 Sensing. *J. Phys. Chem. C* 2015, *119*, 26164–26170.
18. Chen, S.; Yuan, R.; Chai, Y.; Hu, F. Electrochemical sensing of hydrogen peroxide using metal nanoparticles: A review. *Microchim. Acta* **2013**, *180*, 15–32, doi:10.1007/s00604-012-0904-4.
19. Hsu, Y.K.; Chen, Y.C.; Lin, Y.G. Spontaneous formation of CuO nanosheets on Cu foil for H 2 O 2 detection. *Appl. Surf. Sci.* **2015**, *354*, 85–89, doi:10.1016/j.apsusc.2015.05.141.
20. Huang, J.; Zhu, Y.; Zhong, H.; Yang, X.; Li, C. Dispersed CuO nanoparticles on a silicon nanowire for improved performance of nonenzymatic H2O2 detection. *ACS Appl. Mater. Interfaces* **2014**, *6*, 7055–7062, doi:10.1021/am501799w.
21. Wang, M.; Ma, J.; Guan, X.; Peng, W.; Fan, X.; Zhang, G.; Zhang, F.; Li, Y. A novel H2O2 electrochemical sensor based on NiCo2S4 functionalized reduced graphene oxide. *J. Alloys Compd.* **2019**, *784*, 827–833, doi:10.1016/j.jallcom.2019.01.043.
22. Ma, M.; Zhang, Y.; Gu, N. Peroxidase-like catalytic activity of cubic Pt nanocrystals. *Colloids Surfaces A Physicochem. Eng. Asp.* **2011**, *373*, 6–10, doi:10.1016/j.colsurfa.2010.08.007.
23. Li, Y.; Jia, W.Z.; Song, Y.Y.; Xia, X.H. Superhydrophobicity of 3D porous copper films prepared using the hydrogen bubble dynamic template. *Chem. Mater.* **2007**, *19*, 5758–5764, doi:10.1021/cm071738j.

24. Sahoo, R.K.; Das, A.; Samantaray, K.; Singh, S.K.; Mane, R.S.; Shin, H.C.; Yun, J.M.; Kim, K.H. Electrochemical glucose sensing characteristics of two-dimensional faceted and non-faceted CuO nanoribbons. *CrystEngComm* **2019**, *21*, 1607–1616, doi:10.1039/C8CE02033G.
25. Walid, A.; Hocine, G.; Beniaiche, A. Effect of deposition time on the properties of zinc oxide thin films produced via electrochemical method. **2016**, *01001*, 1–6.
26. Xu, J.F.; Ji, W.; Shen, Z.X.; Li, W.S.; Tang, S.H.; Ye, X.R.; Jia, D.Z.; Xin, X.Q. Raman spectra of CuO nanocrystals. *J. Raman Spectrosc.* **1999**, *30*, 413–415, doi:10.1002/(SICI)1097-4555(199905)30:5<413::AID-JRS387>3.0.CO;2-N.
27. Yu, T.; Zhao, X.; Shen, Z.X.; Wu, Y.H.; Su, W.H. Investigation of individual CuO nanorods by polarized micro-Raman scattering. *J. Cryst. Growth* **2004**, *268*, 590–595, doi:10.1016/j.jcrysgro.2004.04.097.
28. Ni, Y.; Sun, Z.; Zeng, Z.; Liu, F.; Qin, J. Hydrothermal fabrication of hierarchical CuO nanoflowers for dual-function amperometric sensing of hydrogen peroxide and glucose. *New J. Chem.* **2019**, *43*, 18629–18636, doi:10.1039/c9nj04236a.
29. Chen, L.; Wang, Y.; Hasebe, Y.; Yang, X.; Zhang, D.; Zhang, Z.; Hu, Z. Copper(II) ion-doped polyimide composite for nonenzymatic electrochemical hydrogen peroxide sensing. *Int. J. Electrochem. Sci.* **2019**, *14*, 4891–4902, doi:10.20964/2019.02.61.
30. Wang, Q.; Yang, Y.; Gao, F.; Ni, J.; Zhang, Y.; Lin, Z. Graphene Oxide Directed One-Step Synthesis of Flowerlike Graphene@HKUST-1 for Enzyme-Free Detection of Hydrogen Peroxide in Biological Samples. *ACS Appl. Mater. Interfaces* **2016**, *8*, 32477–32487, doi:10.1021/acsami.6b11965.
31. Zhang, W.; Fan, G.; Yi, H.; Jia, G.; Li, Z.; Yuan, C.; Bai, Y.; Fu, D. Interfacial Engineering of Hierarchical Transition Metal Oxide Heterostructures for Highly Sensitive Sensing of Hydrogen Peroxide. *Small* **2018**, *14*, 1–8, doi:10.1002/smll.201703713.
32. Huang, Z.; Zhang, A.; Zhang, Q.; Pan, S.; Cui, D. Electrochemical Biosensor Based on Dewdrop-Like Platinum Nanoparticles-Decorated Silver Nanoflowers Nanocomposites for H 2 O 2 and Glucose Detection . *J. Electrochem. Soc.* **2019**, *166*, B1138–B1145, doi:10.1149/2.0471913jes.
33. Characterisation and electrochemical behaviour of electrodepositedCu–Fe foams applied as pseudocapacitor electrodes.pdf.
34. Tran, T.H.; Nguyen, V.T. Phase transition of Cu2O to CuO nanocrystals by selective laser heating. *Mater. Sci. Semicond. Process.* **2016**, *46*, 6–9, doi:10.1016/j.mssp.2016.01.021.
35. Fang, J.; Xuan, Y. Investigation of optical absorption and photothermal conversion characteristics of binary CuO/ZnO nanofluids. *RSC Adv.* **2017**, *7*, 56023–56033, doi:10.1039/c7ra12022b.
36. Luo, B.; Li, X.; Yang, J.; Li, X.; Xue, L.; Li, X.; Gu, J.; Wang, M.; Jiang, L. Non-enzymatic electrochemical sensors for the detection of hydrogen peroxide based on Cu2O/Cu nanocomposites. *Anal. Methods* **2014**, *6*, 1114–1120, doi:10.1039/c3ay41914b.
37. Yang, Y.J.; Li, W.; Chen, X. Highly enhanced electrocatalytic oxidation of glucose on Cu (OH) 2/CuO nanotube arrays modified copper electrode. *J. Solid State Electrochem.* **2012**, *16*, 2877–2881, doi:10.1007/s10008-012-1718-3.
38. Choudhary, S.; Sarma, J.V.N.; Pande, S.; Ababou-Girard, S.; Turban, P.; Lepine, B.; Gangopadhyay, S. Oxidation mechanism of thin Cu films: A gateway towards the formation of single oxide phase. *AIP Adv.* **2018**, *8*, doi:10.1063/1.5028407.